Performance Analysis of Reconfigurable Intelligent Surface-Assisted Underwater Wireless Optical Communication Systems

Qi Zhang, Dian-Wu Yue, *Senior Member, IEEE*, and Xian-Ying Xu

***Abstract*—With the in-depth exploration of the ocean, the Internet of Underwater Things (IoUT) technology has attracted increasing attention. Underwater wireless optical communication (UWOC) provides the possibility of massive data transmission for IoUT. The underwater optical link of UWOC can be interrupted by the obstruction of marine animals and plants, seamounts, and some underwater equipment. In this paper, we present a reconfigurable intelligent surface (RIS) assisted UWOC system to solve the problem of link occlusion. The cascaded turbulence channel fading coefficients from source to destination through RIS are modeled as Gamma-Gamma distribution, and the pointing errors caused by beam jitter and RIS jitter are considered. In the RIS-assisted UWOC systems with intensity modulation and direct detection (IM-DD), we apply the approximate distribution of the sum of Gamma-Gamma random variables to derive the probability density function (PDF) of the instantaneous received signal-to-noise ratio (SNR) for the first time. Based on the PDF, the novel closed-form expression of outage probability is given, and the outage probability analysis results show that when the number of reflecting elements is very large (i.e., tends to infinity), the outage probability asymptotically approaches zero. Subsequently, the closed-form expressions of the finite-SNR diversity order, the asymptotical diversity order, and the convergence speed of finite-SNR diversity order to asymptotical diversity order are proposed. Additionally, the ergodic channel capacity expression is investigated. Finally, we give simulation results to validate our derived results and analyze the impacts of the number of reflecting elements of RIS and the pointing errors on the above system performance indicators.**

***Index Terms*—Underwater wireless optical communication, reconfigurable intelligent surface, outage probability, diversity order, ergodic channel capacity.**

I. Introduction

As a promising concept, the Internet of Underwater Things (IoUT) is a powerful technology for realizing the smart ocean. The goal of IoUT is to connect the underwater sensor networks and autonomous underwater vehicles (AUVs) through a stable wireless link to promote seamless underwater operations, such as marine environmental monitoring, oceanographic data collection, seabed resources exploration, rescue and salvage, and so on [1], [2], [3]. Underwater wireless communication (UWC) in IoUT can transmit data by using wireless carriers, i.e. acoustic wave, radio frequency (RF) wave, and optical wave [4], [5]. Although acoustic signals can propagate over long distances with small signal attenuation, they usually have low bandwidth (typically on the order of Kbps), high delay, poor directivity and may affect marine organisms. On the other hand, RF signals support higher data rates (typically on the order of Mbps) and have low power consumption, but at the expense of decreased communication range and high signal attenuation. Compared with underwater acoustic and radio frequency communications, underwater wireless optical communication (UWOC) has the lowest link delay, the highest transmission rate (typically on the order of Gbps), and the lowest implementation cost. It is particularly well-suited to high-speed and large-capacity underwater data transmission [4], [5]. Moreover, UWOC can be combined with the existing RF communications to establish mixed RF-UWOC systems for realizing the information transmission between the IoUT and other platforms. For example, [6] studied a dual-hop RF-UWOC transmission system and analyzed the outage probability and bit error rate (BER). The secrecy performance for a dual-hop mixed RF-UWOC system was discussed in [7] and [8]. In conclusion, UWOC shows broad application prospects in IoUT systems.

UWOC systems require that the transmitting light source and the receiving detector must be aligned. Considering the high transmission rate of UWOC, even short-term blocking or occlusion can lead to sudden communication interruption, resulting in the loss of large amounts of transmission information. This situation is fatal to a reliable IoUT system. In the underwater environment, marine animals and plants, seamounts, and offshore platform equipment can occlude or block the optical link between the light source and the detector, increasing the possibility of optical information loss. The emerging concept of reconfigurable intelligent surfaces (RISs) opens the door for reducing the adverse effects of obstacles and blockages on underwater wireless optical links.

RIS is a new and revolutionary technology that was initially used for RF communication links. Specifically, the RIS is a planar surface including multiple low-cost passive reflecting elements, each of which can independently control the amplitude

Manuscript received 26 March 2024; revised 16 May 2024; accepted 28 May 2024. Date of publication 31 May 2024; date of current version 10 June 2024. This work was supported in part by the National Natural Science Foundation of China under Grant 62301108 and in part by the Science and Technology Program of Liaoning Province under Grant 2023JH26/10300010. *(Corresponding author: Dian-Wu Yue.)*

Qi Zhang and Dian-Wu Yue are with the College of Information Science and Technology, Dalian Maritime University, Dalian 116026, China (e-mail: zhangqi0081@dlmu.edu.cn; dwyue@dlmu.edu.cn).

Xian-Ying Xu is with the School of Information Science and Engineering, Dalian Polytechnic University, Dalian 116034, China (e-mail: xuxiany@dlpu.edu.cn).

Digital Object Identifier 10.1109/JPHOT.2024.3407882

and/or phase changes of the incident signals [9]. It is used to reconfigure the wireless propagation environment through software-controlled reflection [9]. This technology can be used in beyond 5 G and 6 G RF mobile communication systems [10], [11], [12], [13], [14]. RIS for optical communications is different from that for RF communications. The hardware implementation of RIS for optical signals can be divided into three main categories, namely, metasurface-, mirror array-, and liquid crystal-based RIS [15].

At present, RISs for optical signals are mainly used in indoor visible light communications (VLC) and free space optical communications (FSOC). For instance, considering metasurface-based and mirror array-based RIS models, [16] studied the temporal characteristics of the RIS-based indoor VLC channel using radiometric concepts. [17] devoted to investigating the effect of VLC RIS and putting forward a joint resource management method for a RIS-aided VLC system to maximize the overall spectral efficiency. [18] investigated physical layer security in a RIS-aided VLC system with multiple legitimate users and one eavesdropper. [19] designed a RIS-assisted system to improve the coverage of hybrid VLC/RF indoor wireless communication. Recently, the liquid crystal-based RIS has been studied in the VLC system. [20] proposed for the first time the concept of receivers using tunable liquid crystal-based RIS in VLC. In [21], a liquid crystal RIS-based VLC receiver design was proposed, and its operating principles and the channel model for a VLC system with such a receiver were provided.

For the RIS-assisted FSOC system, some research results are also presented. In [22], with the aim to increase the communication coverage and improve the system performance, RISs are considered in an FSOC setup, in which both atmospheric turbulence and pointing errors are considered. Considering link distances and jitter ratios at the RIS position, [23] carried out a performance analysis of RIS-aided FSOC links. In [24], a controllable multi-branch FSOC system based on optical RISs was proposed, and the asymptotic average BER and the outage probability were derived. [25] reported the performance analysis of multiple RISs-assisted FSOC and investigated the symbol error rate (SER) performance by utilizing the selection of the best RIS from the multiple available RISs.

Although some work has been done on RISs for optical signals in VLC and FSOC, research on RIS-assisted underwater communication systems still needs to be made available [26], [27]. [28] proposed a RIS-assisted dual-hop mixed RF-UWOC system, but RIS is used in the RF link. [26] brought the concept of RIS to UWOC links, and the central limit theorem was applied for performance evaluation. [27] studied the outage probability over log-normal channels in a RIS-assisted UWOC system. In an underwater environment, ocean turbulence has a strong impact on the performance of UWOC systems. Turbulence fading is not considered in the indoor VLC [16], [17], [18], [19], [20], [21], so the results of VLC are not applicable to UWOC systems. Further, we have summarized the contributions of existing research related to the RIS-assisted FSOC and UWOC systems in Table I. From Table I, some works consider the single-reflecting element RIS [23], [24]. Compared with single-reflecting element RIS, the modeling and analysis of multi-reflecting element RIS channel are more challenging. In existing works of [22] and [26], the central limit theorem is commonly used to analyze the channel of multi-reflecting element RIS. However, the results obtained by the central limit theorem are only suitable for the case with a large number of reflecting elements. For the case with a small number of RIS reflecting elements, the results revealed that the difference between the analytical and simulation results is very large, and it is difficult to evaluate the system performance accurately.

TABLE I
EXISTING RESEARCH ON RIS-ASSISTED FSOC AND UWOC SYSTEMS

Reference	Contributions
[22]	Derived closed-form expressions of the outage probability, average BER, and channel capacity for FSOC systems by assuming a large number of reflecting elements at the RIS and using the central limit theorem.
[23]	Applied the single-reflecting element RIS to FSOC systems. Evaluated the system performance through the outage probability, ergodic capacity, and average BER.
[24]	Derived closed-form expressions for asymptotic average BER and the outage probability for RIS-assisted FSOC systems without considering atmospheric turbulence fading.
[25]	Derived the closed-form expression of average SER for RIS-assisted FSOC systems with RIS selection.
[26]	Analyzed the BER, outage probability, and channel capacity for RIS-assisted UWOC systems by using the central limit theorem.
[27]	Derived the closed-form expression of outage probability for RIS-assisted UWOC systems over log-normal channels.

Against the above background, we establish the multi-reflecting element RIS-assisted UWOC system model in the environment with obstacles, and the fading coefficients of the cascaded turbulence channels from source to destination through RIS are modeled as Gamma-Gamma distribution. To the best of our knowledge, such a system setup in conjunction with the proposed analysis has not yet been investigated. The contributions made by this paper are enumerated below:

- We present a general framework to analyze the performance of the multi-reflecting element RIS-assisted UWOC systems. In addition, the ocean turbulence fading and the pointing errors caused by beam jitter and RIS jitter are considered.
- For the RIS-assisted UWOC systems, the probability density function (PDF) of instantaneous SNR has been derived by using a novel method, i.e., the one with the approximate distribution of the sum of Gamma-Gamma random variables. Unlike the results obtained by the central limit theorem, the derivation results based on the approximate distribution method can accurately evaluate the system performance and are not limited by the number of reflecting elements.
- Novel closed-form expressions quantifying the outage probability, the finite-SNR diversity order, the asymptotical diversity order, the convergence speed of finite-SNR diversity order to asymptotical diversity order, and the ergodic capacity of the RIS-assisted UWOC systems have been derived. Notably, this is the first time to evaluate the finite-SNR diversity order and its convergence speed in RIS-assisted wireless optical communication systems.

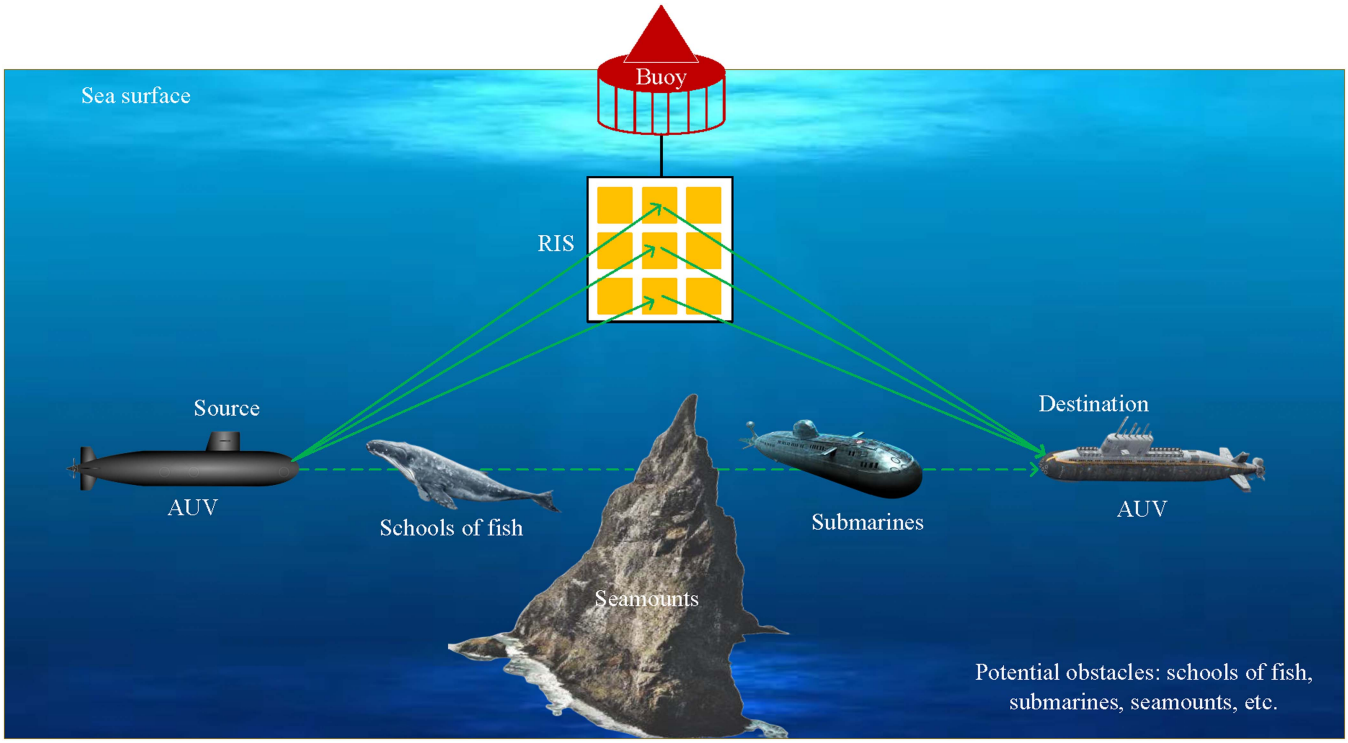

Fig. 1. System model for a RIS-assisted UWOC system.

- The accuracy of the expressions derived in the paper has been verified using Monte Carlo simulation. The effects of the number of reflecting elements and pointing errors on the considered system have been analyzed quantitatively.

The rest of the paper is organized as follows: Section II describes the system and channel model of the RIS-assisted UWOC system. The system performance analysis is given in Section III. In Section IV, the simulation results are investigated. Finally, the conclusions are shown in Section V.

II. System and Channel Models

As illustrated in Fig. 1, we propose a RIS-assisted UWOC communication system composed of an optical source, an optical RIS, and a destination. Due to the obstacles, such as the schools of fish, submarines, and seamounts, the line-of-sight (LOS) link (i.e., direct link) between the source and destination is blocked. The communication is only carried out through the RIS, which can be strategically placed under buoys or fixed on underwater reefs to provide rich non-line-of-sight (NLOS) connections between the source and destination. At present, there are three types of RIS for optical communication, i.e., metasurface-, mirror array-, and liquid crystal-based RISs. As the component of the optical receiver, the liquid crystal-based RISs cannot change the optical channel path. It is mainly used in a short-range indoor VLC system, which is not suitable for the scene we are considering. In this paper, considering optical wireless communication with intensity modulation and direct detection (IM-DD) and according to [24], for the metasurface- and mirror array-based RISs, we can regard these two types of RISs between the input beam and the output beam as a black box from the perspective of the impact on the performance of the optical communication system.

The RIS consists of N reflecting elements. Let x denote the transmission signal from the source with average electric transmission power of P_{te}. The factors that affect the power loss of the received optical signal at the receiver include underwater path loss, turbulence channel fading, and the pointing error caused by the jitter of the transmitter and RIS. Therefore, the received signal at the destination can be written as

$$\begin{aligned} y &= \sum_{n=1}^{N} h_{ln} h_{tn} h_{pn} \rho_n \, x + n_0 \\ &= \sum_{n=1}^{N} \underbrace{h_l^{sr_n} h_l^{r_n d}}_{=h_{ln}} \underbrace{h_t^{sr_n} h_t^{r_n d}}_{=h_{tn}} h_{pn} \rho_n \, x + n_0 \, , \end{aligned} \tag{1}$$

where h_{ln}, h_{tn} and h_{pn} are the path loss, underwater turbulence channel fading, and the channel fading caused by pointing error of the path from the source to the destination through the n^{th} reflecting element, respectively. $\rho_n \in [0, 1]$ is the reflection coefficient of the n^{th} reflecting element. $h_l^{sr_n}$ and $h_l^{r_n d}$ represent the path loss from the source to the n^{th} reflecting element and from the n^{th} reflecting element to the destination, respectively. Similarly, $h_t^{sr_n}$ and $h_t^{r_n d}$ represent the corresponding turbulence fading coefficients of the two paths respectively. $n_0 \sim \mathcal{N}(0, \sigma_n^2)$ is the additive white Gaussian noise (AWGN).

A. Path Loss

In the underwater environment, the path loss is the propagation attenuation of optical signals, which is mainly caused by the absorption and scattering effects of various components of seawater, including water molecules, phytoplankton, non-pigment suspended particles, and colored dissolved organic matter. The general theoretical models of path loss include Beer-Lambert's law and radiative transfer equation (RTE) [4], [5]. RTE can describe the energy conservation of an optical wave passing through a steady medium. However, since the RTE is an integro-differential equation involving independent variables [29], finding an exact analytical solution is very difficult for many practical UWOC applications [4]. Thus, few analytical RTE models have been given in recent years. Compared with RTE, Beer-Lambert's law provides the simplest and most widely used scenario to describe the propagation attenuation of optical signals in the underwater environment. In order to facilitate subsequent analysis, we approximate path loss by the exponential attenuation model of Beer-Lambert's law, which ignores the multiple scattering effect [30].

According to Beer-Lambert's law, we obtain $h_l^i = \exp(-cL_i), i \in \{sr_n,\ r_nd\}$, where c is the extinction coefficient which is the sum of absorption and scattering coefficients. Under the fixed wavelength and a stable water quality environment, c is a constant. L_{sr_n} and L_{r_nd} are link distances from source to the n^{th} reflecting element and from the n^{th} reflecting element to destination, respectively. The separation between reflecting elements is much smaller than the link distance. Then, it can be considered that the link distances from the source to the N reflecting elements are the same, i.e., $L_{sr_n} = L_1$ $(n = 1,\ 2,\ \ldots,\ N)$. Similarly, $L_{r_nd} = L_2$ $(n = 1,\ 2,\ \ldots,\ N)$. Therefore, the path loss coefficient is considered identical for the N paths, and we can get

$$\begin{aligned} h_{ln} &= h_l^{sr_n} h_l^{r_nd} \\ &= \exp\left[-c\left(L_{sr_n} + L_{r_nd}\right)\right] \\ &= \exp\left[-c\left(L_1 + L_2\right)\right] \\ &= h_l\ , \qquad n = 1,\ 2,\ \ldots,\ N\ . \end{aligned} \tag{2}$$

B. Underwater Turbulence

$h_{tn} = h_t^{sr_n} h_t^{r_nd}$ denotes the cascaded turbulence channel fading coefficient from the source to the destination through the n^{th} reflecting element. $h_t^{sr_n}$ and $h_t^{r_nd}$ are characterized by Gamma distribution, and their PDF are given as [31]

$$f_{h_t^{sr_n}}\left(h_t^{sr_n}\right) = \frac{\alpha(\alpha h_t^{sr_n})^{\alpha-1}}{\Gamma(\alpha)} \exp\left(-\alpha h_t^{sr_n}\right)\ , \tag{3}$$

$$f_{h_t^{r_nd}}\left(h_t^{r_nd}\right) = \frac{\beta\left(\beta h_t^{r_nd}\right)^{\beta-1}}{\Gamma(\beta)} \exp\left(-\beta h_t^{r_nd}\right)\ , \tag{4}$$

where $\Gamma(\cdot)$ is the Gamma function, α and β are the turbulence parameters from source to RIS and RIS to destination, respectively. By fixing $h_t^{sr_n}$ and using the change of variable, $h_t^{r_nd} = h_{tn}/h_t^{sr_n}$, the conditional PDF can be obtained as

$$f\left(h_{tn}/h_t^{sr_n}\right) = \frac{\beta(\beta h_{tn}/h_t^{sr_n})^{\beta-1}}{h_t^{sr_n}\Gamma(\beta)} \exp\left(\frac{-\beta h_{tn}}{h_t^{sr_n}}\right)\ . \tag{5}$$

Then, the PDF of h_{tn} can be given as

$$\begin{aligned} l f_{h_{tn}}(h_{tn}) &= \int_0^\infty f\left(h_{tn}/h_t^{sr_n}\right) f_{h_t^{sr_n}}\left(h_t^{sr_n}\right) dh_t^{sr_n} \\ &= \frac{2(\alpha\beta)^{\frac{\alpha+\beta}{2}}}{\Gamma(\alpha)\Gamma(\beta)} h_{tn}^{\frac{(\alpha+\beta)}{2}-1} \mathrm{K}_{\alpha-\beta}\left(2\sqrt{\alpha\beta h_{tn}}\right)\ , \end{aligned} \tag{6}$$

where $\mathrm{K}_p(\cdot)$ is modified Bessel function of the second kind with order p. In (6), we obtain that the cascaded turbulence channel fading coefficient from the source to the destination through the n^{th} reflecting element (i.e., h_{tn}) is modeled by a Gamma-Gamma distribution. $h_{t1},\ h_{t2},\ \ldots,\ h_{tn},\ \ldots,\ h_{tN}$ are independent and identically distributed (i.i.d). Under the assumption of plane wave propagation, the turbulence parameters, α and β, can be calculated as $[\exp(0.225\sigma_{B_i}^2/(1+0.259\sigma_{B_i}^{12/5})^{7/6}) - 1]^{-1}$ [26], [31], where $\sigma_{B_i}^2$ $(i = 1,\ 2)$ represents the Rytov variance of the two paths, which can be given in [32].

C. Pointing Error

In RIS-assisted wireless optical communication systems, h_{pn} is the channel fading coefficient caused by the pointing error of the path from the source to the destination through the n^{th} reflecting element, which is affected by beam jitter and RIS jitter [24]. Beam jitter means that the beam vibrates due to jitter at the source, and RIS jitter refers to the normal vector deflection of the reflecting surface caused by the jitter of the RIS. Since the size of RIS is much smaller than the communication link distance and the reflecting elements are located on the same reflecting surface, they experience identical pointing error. Then, we can get

$$h_{pn} = h_p\ , \qquad n = 1,\ 2,\ \ldots,\ N\ . \tag{7}$$

h_p can be approximated by [33]

$$h_p \approx A_0 \exp\left(-\frac{2R^2}{\omega_{zeq}^2}\right)\ , \qquad R \geq 0\ , \tag{8}$$

and according to the pointing error model in [24], the PDF of h_p can be given as

$$f_{h_p}(h_p) = \frac{\xi^2}{A_0^{\xi^2}} h_p^{\xi^2-1}\ , \qquad 0 \leq h_p \leq A_0\ , \tag{9}$$

where

$$\xi = \sqrt{\frac{\omega_{zeq}^2}{4\sigma_\theta^2(L_1+L_2)^2 + 16\sigma_\phi^2 L_2^2}}\ , \tag{10}$$

and $A_0 = [\mathrm{erf}(v_0)]^2$ is the fraction of the collected power at $R = 0$, R is the pointing error radial displacement at the receiver, $\omega_{zeq} = \omega_z\sqrt{\sqrt{\pi}\mathrm{erf}(v_0)/[2v_0\exp(-v_0^2)]}$ is the equivalent beam width, $\mathrm{erf}(\cdot)$ is the error function, $v_0 = \sqrt{\pi/2}D_R/\omega_z$, D_R is receiver aperture radius, and ω_z is the beam width. σ_θ^2 and σ_ϕ^2

are variances of pointing error angle and deflection error angles, respectively.

III. System Performance Analysis

A. PDF of Instantaneous SNR

We assume that all RIS reflecting elements have the same reflection coefficient, that is, $\rho_n = \rho\,(n = 1,\ 2,\ \cdots,\ N)$. Then, the instantaneous SNR can be given as

$$\begin{aligned}\gamma &= \frac{P_{\mathrm{te}}\left(\sum_{n=1}^{N} h_{ln}h_{tn}h_{pn}\rho_n\right)^2}{\sigma_n^2} \\ &= \frac{P_{\mathrm{te}}\rho^2\left(\sum_{n=1}^{N} h_{ln}h_{tn}h_{pn}\right)^2}{\sigma_n^2}\ .\end{aligned} \tag{11}$$

Replacing (2) and (7) in (11), the instantaneous SNR can be expressed as

$$\begin{aligned}\gamma &= \frac{P_{\mathrm{te}}\rho^2 h_l^2 h_p^2\left(\sum_{n=1}^{N} h_{tn}\right)^2}{\sigma_n^2} \\ &= \bar{\gamma}h_p^2\left(\sum_{n=1}^{N} h_{tn}\right)^2 \\ &= \bar{\gamma}h_p^2 h_t^2\ ,\end{aligned} \tag{12}$$

where path loss h_l is deterministic in contrast to h_p and h_t, which are random fading variables. Thus, we let $\bar{\gamma} = P_{\mathrm{te}}\rho^2 h_l^2/\sigma_n^2$ denote fading-free SNR, i.e., average SNR [34], [35]. $h_t = \sum_{n=1}^{N} h_{tn}$ represents the sum of i.i.d. Gamma-Gamma random variables, and its PDF can be calculated as (13), shown at the bottom of this page, but there is no closed-form solution for the multi-dimensional integration in (13). Several methods were used in the literature to obtain approximate solutions. Some of these literatures convert the integration into an infinite sum [36], and some use the central limit theorem to obtain approximate PDF [22], [26]. However, these methods are complex and have limited applications. Here, we apply an alternative method to solve the PDF of h_t.

According to [37], the sum of N identically distributed Gamma-Gamma random variables, i.e., $Y = \sum_{n=1}^{N} X_n$ with $X_n \sim \Gamma\Gamma(\alpha_x, \beta_x, \Omega_x)$ ($\Gamma\Gamma(\cdot)$ denotes Gamma-Gamma distribution), can be accurately approximated by another Gamma-Gamma random variable with parameters $(\alpha_y, \beta_y, \Omega_y)$ [37]. The parameters are given by

$$\alpha_y = g\alpha_x\ ,\qquad \beta_y = g\beta_x\ ,\qquad \Omega_y = N\Omega_x\ , \tag{14}$$

where

$$g = N\left(1 + \frac{2}{N}\sum_{n=1}^{N}\sum_{m=n+1}^{N}\mu_{nm}\right)^{-1}\ , \tag{15}$$

and μ_{nm} is the correlation coefficient between X_n and X_m.

Since $h_{t1},\ h_{t2},\ \ldots,\ h_{tn},\ \ldots,\ h_{tN}$ are independent and identically distributed, the correlation coefficient between h_{tn} and h_{tm} is zero, and we have $h_{tn} \sim \Gamma\Gamma(\alpha, \beta, 1)$ from (6). Therefore, according to (14) and (15), we obtain

$$h_t = \sum_{n=1}^{N} h_{tn} \sim \Gamma\Gamma\left(\alpha_h, \beta_h, N\right)\ , \tag{16}$$

where $\alpha_h = N\alpha$ and $\beta_h = N\beta$. Then, the PDF of h_t can be expressed as

$$\begin{aligned}f_{h_t}(h_t) = &\frac{2\left(\frac{\alpha_h\beta_h}{N}\right)^{\frac{\alpha_h+\beta_h}{2}}}{\Gamma(\alpha_h)\,\Gamma(\beta_h)}h_t^{\frac{\alpha_h+\beta_h}{2}-1} \\ &\times \mathrm{K}_{\alpha_h-\beta_h}\left(2\sqrt{\frac{\alpha_h\beta_h}{N}h_t}\right)\ .\end{aligned} \tag{17}$$

For the convenience of subsequent calculation, we use Eq. (03.04.26.0009.01) in [38] to rewrite the Bessel function in (17) as

$$\begin{aligned}&\mathrm{K}_{\alpha_h-\beta_h}\left(2\sqrt{\frac{\alpha_h\beta_h}{N}h_t}\right) \\ &= \frac{1}{2}G_{0,2}^{2,0}\left(\frac{\alpha_h\beta_h}{N}h_t\,\middle|\,\begin{matrix}\cdots \\ \frac{\alpha_h-\beta_h}{2}, \frac{\beta_h-\alpha_h}{2}\end{matrix}\right)\ ,\end{aligned} \tag{18}$$

where $G_{p,q}^{m,n}(\cdot|\cdot)$ is Meijer-G function. Substituting (18) into (17), we obtain (19) shown at the bottom of the next page. Then, the property of Meijer-G function of Eq. (07.34.16.0001.01) in [38] is used within (19), it can be calculated as

$$\begin{aligned}f_{h_t}(h_t) = &\frac{\alpha_h\beta_h}{N\Gamma(\alpha_h)\,\Gamma(\beta_h)} \\ &\times G_{0,2}^{2,0}\left(\frac{\alpha_h\beta_h}{N}h_t\,\middle|\,\begin{matrix}\cdots \\ \alpha_h-1, \beta_h-1\end{matrix}\right)\ .\end{aligned} \tag{20}$$

Let $h = h_p h_t$ denote the joint channel fading coefficient and the PDF of h can be calculated as

$$\begin{aligned}f_h(h) &= \int_0^{A_0} f_{h_p}(h_p)\, f_{h|h_p}(h\,|h_p)\, dh_p \\ &= \int_0^{A_0} \frac{1}{h_p} f_{h_p}(h_p)\, f_{h_t}\left(\frac{h}{h_p}\right) dh_p\ ,\end{aligned} \tag{21}$$

where $f_{h|h_p}(h|h_p)$ is the conditional PDF. Substituting (9) and (20) into (21), we can obtain (22), shown at the bottom

$$\begin{aligned}&f_{h_t}(h_t) \\ &= \int_0^{\infty}\int_0^{\infty}\cdots\int_0^{\infty} f_{h_{t1}}(h_{t1}) f_{h_{t2}}(h_{t2})\cdots f_{h_{t(N-1)}}\left(h_{t(N-1)}\right) f_{h_{tN}}\left(h_t - \sum_{n=1}^{N-1} h_{tn}\right) dh_{t1}dh_{t2}\cdots dh_{t(N-1)}\ .\end{aligned} \tag{13}$$

of this page. For the Meijer-G function in (22), the variable h_p appears at the denominator. To obtain a Meijer-G function with a numerator-based variable h_p, we utilize the reflection property of the Meijer-G function shown as Eq. (07.34.16.0002.01) in [38], and we have

$$\begin{aligned} &G_{0,2}^{2,0}\left(\frac{\alpha_h\beta_h h}{N h_p}\middle|\begin{matrix}\cdots\\ \alpha_h-1,\beta_h-1\end{matrix}\right)\\ &=G_{2,0}^{0,2}\left(\frac{N h_p}{\alpha_h\beta_h h}\middle|\begin{matrix}2-\alpha_h,2-\beta_h\\ \cdots\end{matrix}\right). \end{aligned} \tag{23}$$

Replacing (23) in (22), we can obtain (24) shown at the bottom of this page. Then, we solve the integration of (24) with the help of Eq. (07.34.21.0084.01) in [38] and apply the reflection property of the Meijer-G function to get a Meijer-G function with a numerator-based variable h. Consequently, the PDF of h can be expressed as

$$\begin{aligned} f_h(h)=&\frac{\alpha_h\beta_h\xi^2}{N\Gamma(\alpha_h)\Gamma(\beta_h)A_0}\\ &\times G_{1,3}^{3,0}\left(\frac{\alpha_h\beta_h h}{N A_0}\middle|\begin{matrix}\xi^2\\ \xi^2-1,\alpha_h-1,\beta_h-1\end{matrix}\right). \end{aligned} \tag{25}$$

Based on $f_h(h)$, the PDF of instantaneous SNR $\gamma=\bar{\gamma}h^2$ can be calculated as

$$f_\gamma(\gamma)=f_h\left(\sqrt{\frac{\gamma}{\bar{\gamma}}}\right)\left|\frac{dh}{d\gamma}\right|=f_h\left(\sqrt{\frac{\gamma}{\bar{\gamma}}}\right)\left(\frac{1}{2\sqrt{\bar{\gamma}\gamma}}\right). \tag{26}$$

Substituting (25) into (26), the closed-form expression of $f_\gamma(\gamma)$ can be obtained as (27) shown at the bottom of this page.

B. Outage Probability

Since the coherence time of the underwater optical turbulence channel is long ($10^{-5}\sim10^{-2}$ second [39]), it exhibits quasi-static characteristics [40]. For a typical transmission rate of hundreds of megabits per second, fading remains constant over thousands of consecutive bits or even more. Therefore, the communication link may be temporarily interrupted due to deep fading. For the quasi-static channel, outage probability is a more appropriate performance metric than BER [40].

The outage probability is defined as the probability that the instantaneous SNR γ is lower than the threshold SNR $\gamma_{\rm th}$. It can be given by

$$P_{\rm out}=\int_0^{\gamma_{\rm th}} f_\gamma(\gamma)\,d\gamma. \tag{28}$$

Substituting (27) into (28), we have the integral equation shown in (29) shown at the bottom of the next page. Using the integration of Meijer-G function of Eq. (07.34.21.0084.01) in [38], the closed-form expression of outage probability can be expressed as (30) shown at the bottom of the next page, where $\mathbf{b}=[\frac{\xi^2-1}{2},\frac{\xi^2}{2},\frac{\alpha_h-1}{2},\frac{\alpha_h}{2},\frac{\beta_h-1}{2},\frac{\beta_h}{2}]$.

Further, we investigate the outage probability when the number of reflecting elements is large, i.e., $N\to\infty$. In this case, the inner argument of the Meijer-G function in (30) tends to infinity, i.e., $\alpha_h^2\beta_h^2\gamma_{\rm th}/(16N^2A_0^2\bar{\gamma})=N^2\alpha^2\beta^2\gamma_{\rm th}/(16A_0^2\bar{\gamma})\to\infty$. Utilizing Eq. (07.34.06.0018.01) in [38], the Meijer-G function can be expanded, and $P_{\rm out}(N)_{N\to\infty}$ can be expressed as (31) shown at the bottom of the next page. When $N\to\infty$, we have $(N\alpha+1)/2\approx N\alpha/2$, and applying the recursive property of the Gamma function, i.e., $\Gamma(1+x)=x\Gamma(x)$, (31) can be simplified as

$$\underset{N\to\infty}{P_{\rm out}(N)}\approx\frac{2^{N\alpha+N\beta-2}\left(\Gamma\left(\frac{N\alpha}{2}\right)\right)^2\left(\Gamma\left(\frac{N\beta}{2}\right)\right)^2}{\pi\Gamma(N\alpha)\Gamma(N\beta)}. \tag{32}$$

According to the asymptotic series expansion of Gamma function, i.e., $\Gamma(x)_{x\to\infty}\approx\sqrt{2\pi}x^{x-\frac{1}{2}}\exp(-x)$, we have

$$\Gamma\left(\frac{N\Delta}{2}\right)\approx\sqrt{2\pi}\left(\frac{N\Delta}{2}\right)^{\frac{N\Delta-1}{2}}\exp\left(-\frac{N\Delta}{2}\right), \tag{33}$$

$$\begin{aligned} f_{h_t}(h_t)&=\frac{\left(\frac{\alpha_h\beta_h}{N}\right)^{\frac{\alpha_h+\beta_h}{2}}}{\Gamma(\alpha_h)\Gamma(\beta_h)}h_t^{\frac{\alpha_h+\beta_h}{2}-1}G_{0,2}^{2,0}\left(\frac{\alpha_h\beta_h}{N}h_t\middle|\begin{matrix}\cdots\\ \frac{\alpha_h-\beta_h}{2},\frac{\beta_h-\alpha_h}{2}\end{matrix}\right)\\ &=\frac{\alpha_h\beta_h}{N\Gamma(\alpha_h)\Gamma(\beta_h)}\left(\frac{\alpha_h\beta_h}{N}h_t\right)^{\frac{\alpha_h+\beta_h}{2}-1}G_{0,2}^{2,0}\left(\frac{\alpha_h\beta_h}{N}h_t\middle|\begin{matrix}\cdots\\ \frac{\alpha_h-\beta_h}{2},\frac{\beta_h-\alpha_h}{2}\end{matrix}\right). \end{aligned} \tag{19}$$

$$f_h(h)=\frac{\alpha_h\beta_h\xi^2}{N\Gamma(\alpha_h)\Gamma(\beta_h)A_0^{\xi^2}}\int_0^{A_0}h_p^{\xi^2-2}G_{0,2}^{2,0}\left(\frac{\alpha_h\beta_h h}{N h_p}\middle|\begin{matrix}\cdots\\ \alpha_h-1,\beta_h-1\end{matrix}\right)dh_p. \tag{22}$$

$$f_h(h)=\frac{\alpha_h\beta_h\xi^2}{N\Gamma(\alpha_h)\Gamma(\beta_h)A_0^{\xi^2}}\int_0^{A_0}h_p^{\xi^2-2}G_{2,0}^{0,2}\left(\frac{N h_p}{\alpha_h\beta_h h}\middle|\begin{matrix}2-\alpha_h,2-\beta_h\\ \cdots\end{matrix}\right)dh_p. \tag{24}$$

$$f_\gamma(\gamma)=\frac{\alpha_h\beta_h\xi^2}{2N\Gamma(\alpha_h)\Gamma(\beta_h)A_0\sqrt{\bar{\gamma}\gamma}}G_{1,3}^{3,0}\left(\frac{\alpha_h\beta_h}{N A_0}\sqrt{\frac{\gamma}{\bar{\gamma}}}\middle|\begin{matrix}\xi^2\\ \xi^2-1,\alpha_h-1,\beta_h-1\end{matrix}\right). \tag{27}$$

$$\Gamma(N\Delta) \approx \sqrt{2\pi}(N\Delta)^{N\Delta-\frac{1}{2}} \exp(-N\Delta) , \quad (34)$$

where $\Delta \in \{\alpha, \beta\}$. Substituting (33) and (34) into (32), we get

$$\underset{N\to\infty}{P_{\text{out}}(N)} \to \frac{2}{N\sqrt{\alpha\beta}} \to 0 . \quad (35)$$

From (35), we theoretically obtain and prove that if the number of reflecting elements is very large (i.e., tends to infinity), the outage probability asymptotically approaches zero.

In addition, we define the outage probability performance gain as

$$G(N) = \frac{P_{\text{out}}(N)}{P_{\text{out}}(N+1)} . \quad (36)$$

By analyzing the relationship between $G(N)$ and N, the performance gain brought by increasing the number of reflecting elements can be obtained.

C. Diversity Order and Its Convergence Speed

In this subsection, we consider the finite-SNR diversity order, the asymptotical diversity order under high-SNR, and the convergence speed of finite-SNR diversity order to asymptotical diversity order. While the asymptotic analysis proposed in earlier studies is important for understanding the maximum diversity order, such diversity order may not be available in the actual range of SNR. Furthermore, different systems with the same asymptotical diversity order may have different diversity gains in the range of finite SNR values. These motivate the analysis of finite-SNR diversity gain. Therefore, in addition to the asymptotic diversity order, we derive the closed-form expressions of the finite-SNR diversity order and its convergence speed in the RIS-assisted wireless optical communication systems for the first time.

Diversity order is the negative slope of the outage probability curve on a log-log scale, which determines how fast the outage probability changes with SNR. The finite-SNR diversity order is defined as [40]

$$\text{DO}(\bar{\gamma}) = -\frac{\partial \ln P_{\text{out}}(\bar{\gamma})}{\partial \ln \bar{\gamma}} . \quad (37)$$

Substituting (30) into (37), we obtain

$$\text{DO}(\bar{\gamma}) = \frac{1}{2} - \frac{\partial \ln \Psi(\bar{\gamma})}{\partial \ln \bar{\gamma}} , \quad (38)$$

where

$$\Psi(\bar{\gamma}) = G_{3,7}^{6,1}\left(\frac{\alpha_h^2\beta_h^2\gamma_{\text{th}}}{16N^2A_0^2\bar{\gamma}} \middle| \begin{matrix} \frac{1}{2}, \frac{\xi^2}{2}, \frac{\xi^2+1}{2} \\ \mathbf{b}, -\frac{1}{2} \end{matrix}\right) . \quad (39)$$

In (38), we have

$$\frac{\partial \ln \Psi(\bar{\gamma})}{\partial \ln \bar{\gamma}} = \frac{\bar{\gamma}}{\Psi(\bar{\gamma})}\frac{\partial \Psi(\bar{\gamma})}{\partial \bar{\gamma}} . \quad (40)$$

With the help of the derivative of Meijer-G function of Eq. (07.34.20.0002.01) in [38] along with the chain rule of differentiation, we can get

$$\frac{\partial \Psi(\bar{\gamma})}{\partial \bar{\gamma}} = -\frac{1}{\bar{\gamma}} G_{4,8}^{6,2}\left(\frac{\alpha_h^2\beta_h^2\gamma_{\text{th}}}{16N^2A_0^2\bar{\gamma}} \middle| \begin{matrix} 0, \frac{1}{2}, \frac{\xi^2}{2}, \frac{\xi^2+1}{2} \\ \mathbf{b}, 1, -\frac{1}{2} \end{matrix}\right) . \quad (41)$$

Substituting (39) and (41) into (40) and replacing (40) in (38), we obtain the closed-form expression of the finite-SNR diversity order as

$$\text{DO}(\bar{\gamma}) = \frac{1}{2} + \frac{G_{4,8}^{6,2}\left(\frac{\alpha_h^2\beta_h^2\gamma_{\text{th}}}{16N^2A_0^2\bar{\gamma}} \middle| \begin{matrix} 0, \frac{1}{2}, \frac{\xi^2}{2}, \frac{\xi^2+1}{2} \\ \mathbf{b}, 1, -\frac{1}{2} \end{matrix}\right)}{G_{3,7}^{6,1}\left(\frac{\alpha_h^2\beta_h^2\gamma_{\text{th}}}{16N^2A_0^2\bar{\gamma}} \middle| \begin{matrix} \frac{1}{2}, \frac{\xi^2}{2}, \frac{\xi^2+1}{2} \\ \mathbf{b}, -\frac{1}{2} \end{matrix}\right)} . \quad (42)$$

In the following, we consider asymptotically high-SNR to derive the diversity order, i.e., asymptotical diversity order (ADO), which is defined as

$$\text{ADO} = \underset{\bar{\gamma}\to\infty}{\text{DO}}(\bar{\gamma}) = -\frac{\partial \ln\left[\underset{\bar{\gamma}\to\infty}{P_{\text{out}}(\bar{\gamma})}\right]}{\partial \ln \bar{\gamma}} . \quad (43)$$

Under the assumption of high-SNR, i.e., $\bar{\gamma} \to \infty$, the inner argument of Meijer-G function in (30) goes to zero, i.e., $\alpha_h^2\beta_h^2\gamma_{\text{th}}/(16N^2A_0^2\bar{\gamma}) \to 0$. Then, applying Eq. (07.34.06.0006.01) in [38] and the recursive property of the Gamma function, the Meijer-G function can be expanded into

$$P_{\text{out}} = \frac{\alpha_h\beta_h\xi^2}{2N\Gamma(\alpha_h)\Gamma(\beta_h)A_0\sqrt{\bar{\gamma}}} \int_0^{\gamma_{\text{th}}} \gamma^{-\frac{1}{2}} G_{1,3}^{3,0}\left(\frac{\alpha_h\beta_h}{NA_0\sqrt{\bar{\gamma}}}\gamma^{\frac{1}{2}} \middle| \begin{matrix} \xi^2 \\ \xi^2-1, \alpha_h-1, \beta_h-1 \end{matrix}\right) d\gamma . \quad (29)$$

$$P_{\text{out}} = \frac{2^{\alpha_h+\beta_h-5}\alpha_h\beta_h\xi^2}{\pi N\Gamma(\alpha_h)\Gamma(\beta_h)A_0}\left(\frac{\gamma_{\text{th}}}{\bar{\gamma}}\right)^{\frac{1}{2}} G_{3,7}^{6,1}\left(\frac{\alpha_h^2\beta_h^2\gamma_{\text{th}}}{16N^2A_0^2\bar{\gamma}} \middle| \begin{matrix} \frac{1}{2}, \frac{\xi^2}{2}, \frac{\xi^2+1}{2} \\ \mathbf{b}, -\frac{1}{2} \end{matrix}\right) . \quad (30)$$

$$\underset{N\to\infty}{P_{\text{out}}(N)} = \frac{2^{N\alpha+N\beta-5}N\alpha\beta\xi^2}{\pi\Gamma(N\alpha)\Gamma(N\beta)A_0}\left(\frac{\gamma_{\text{th}}}{\bar{\gamma}}\right)^{\frac{1}{2}} \frac{\prod_{j=1}^{6}\Gamma\left(\frac{1}{2}+b_j\right)}{\Gamma(1)\Gamma\left(\frac{\xi^2+1}{2}\right)\Gamma\left(\frac{\xi^2}{2}+1\right)}\left(\frac{N^2\alpha^2\beta^2\gamma_{\text{th}}}{16A_0^2\bar{\gamma}}\right)^{-\frac{1}{2}} . \quad (31)$$

the form of a sum of multiple terms. Therefore, $P_{\text{out}}(\bar{\gamma})_{\bar{\gamma}\to\infty}$ can be written as (44) shown at the bottom of this page. From (44), when $\bar{\gamma}\to\infty$, the highest order term of $\bar{\gamma}$ dominates the outage probability. Thus, the lower order terms can be ignored, then (44) can be simplified as (45) shown at the bottom of this page, where $\min(\cdot)$ denotes the minimum value. Substituting (45) into (43), we get the expression of asymptotical diversity order as

$$\begin{aligned}\text{ADO} &= \frac{1}{2}+\min\left(\mathbf{b}\right)\\ &= \frac{1}{2}\min\left(\xi^2,\alpha_h,\beta_h\right)\\ &= \frac{1}{2}\min\left(\xi^2,N\alpha,N\beta\right)\ .\end{aligned}\tag{46}$$

Let us make some comments on the diversity order of the proposed system.

1) The asymptotical diversity order under high-SNR depends not only upon the turbulence parameters but also on the pointing error and the number of reflecting elements.

2) If $\xi^2 > N\min(\alpha,\beta)$, then $\text{ADO}=\frac{N}{2}\min(\alpha,\beta)$. Therefore, the asymptotical diversity order is dominated by the number of reflecting elements and the minimum turbulence parameter.

3) If the number of reflecting elements increases, resulting in $\xi^2 < N\min(\alpha,\beta)$, then $\text{ADO}=\frac{\xi^2}{2}$. Hence, the asymptotical diversity order is dominated only by the pointing error. If the number of reflecting elements continues to increase, the asymptotical diversity order will remain the same.

Here, it is important to note that the asymptotical diversity order of (46) is obtained if all reflecting channels experience identical pointing error, which is justified from a practical point of view.

In addition, the convergence speed of finite-SNR diversity order to asymptotical diversity order is an important indicator for evaluating the diversity order performance of the system [41], [42]. The convergence speed (CS) can be obtained by normalizing the gradual change in the finite-SNR diversity order with respect to the asymptotical diversity order. Mathematically speaking, it can be defined as

$$\text{CS}\left(\bar{\gamma}\right) = -\frac{1}{\text{ADO}}\frac{\partial^2\ln P_{\text{out}}\left(\bar{\gamma}\right)}{\partial\left(\ln\bar{\gamma}\right)^2} = \frac{1}{\text{ADO}}\frac{\partial\text{DO}\left(\bar{\gamma}\right)}{\partial\ln\bar{\gamma}}\ .\tag{47}$$

According to (42), we get

$$\frac{\partial\text{DO}\left(\bar{\gamma}\right)}{\partial\ln\bar{\gamma}} = \bar{\gamma}\frac{\partial\text{DO}\left(\bar{\gamma}\right)}{\partial\bar{\gamma}} = \bar{\gamma}\frac{\partial\left[\dfrac{\Upsilon\left(\bar{\gamma}\right)}{\Psi\left(\bar{\gamma}\right)}\right]}{\partial\bar{\gamma}}\ ,\tag{48}$$

where

$$\Upsilon\left(\bar{\gamma}\right) = G_{4,8}^{6,2}\left(\frac{\alpha_h^2\beta_h^2\gamma_{\text{th}}}{16N^2A_0^2\bar{\gamma}}\,\middle|\,\begin{matrix}0,\frac{1}{2},\frac{\xi^2}{2},\frac{\xi^2+1}{2}\\ \mathbf{b},1,-\frac{1}{2}\end{matrix}\right)\ ,\tag{49}$$

and we have

$$\frac{\partial\left[\dfrac{\Upsilon\left(\bar{\gamma}\right)}{\Psi\left(\bar{\gamma}\right)}\right]}{\partial\bar{\gamma}} = \frac{\Psi\left(\bar{\gamma}\right)\dfrac{\partial\Upsilon\left(\bar{\gamma}\right)}{\partial\bar{\gamma}} - \Upsilon\left(\bar{\gamma}\right)\dfrac{\partial\Psi\left(\bar{\gamma}\right)}{\partial\bar{\gamma}}}{\left[\Psi\left(\bar{\gamma}\right)\right]^2}\ .\tag{50}$$

Using the derivative of Meijer-G function of Eq. (07.34.20.0002.01) in [38] along with the chain rule of differentiation, we obtain

$$\frac{\partial\Upsilon\left(\bar{\gamma}\right)}{\partial\bar{\gamma}} = -\frac{1}{\bar{\gamma}}G_{5,9}^{6,3}\left(\frac{\alpha_h^2\beta_h^2\gamma_{\text{th}}}{16N^2A_0^2\bar{\gamma}}\,\middle|\,\begin{matrix}0,0,\frac{1}{2},\frac{\xi^2}{2},\frac{\xi^2+1}{2}\\ \mathbf{b},1,1,-\frac{1}{2}\end{matrix}\right)\ .\tag{51}$$

Then, Substituting (41) and (51) into (50) and sorting out (47), (48) and (50), we obtain the closed-form expression of the convergence speed as (52) shown at the bottom of the next page.

D. Ergodic Channel Capacity

Channel capacity reflects the maximum information transmission rate on the time-varying wireless channel. Ergodic channel capacity can be calculated as

$$C = \int_0^\infty \log_2\left(1+\tau\gamma\right)f_\gamma\left(\gamma\right)d\gamma\ ,\tag{53}$$

where $\tau=\exp(1)/(2\pi)$ for IM-DD scheme. Using Eq. (01.04.26.0003.01) in [38], the logarithm in (53) can be written in Meijer-G function, and we get

$$\begin{aligned}\log_2\left(1+\tau\gamma\right) &= \frac{1}{\ln(2)}\log\left(1+\tau\gamma\right)\\ &= \frac{1}{\ln(2)}G_{2,2}^{1,2}\left(\tau\gamma\,\middle|\,\begin{matrix}1,1\\1,0\end{matrix}\right)\ .\end{aligned}\tag{54}$$

$$P_{\substack{\text{out}\\ \bar{\gamma}\to\infty}}\left(\bar{\gamma}\right) = \frac{2^{\alpha_h+\beta_h-5}\alpha_h\beta_h\xi^2\gamma_{\text{th}}^{\frac{1}{2}}}{\pi N\Gamma\left(\alpha_h\right)\Gamma\left(\beta_h\right)A_0}\sum_{k=1}^{6}\frac{\prod_{j=1,j\neq k}^{6}\Gamma\left(b_j-b_k\right)}{\left(\frac{1}{2}+b_k\right)\Gamma\left(\frac{\xi^2}{2}-b_k\right)\Gamma\left(\frac{\xi^2+1}{2}-b_k\right)}\left(\frac{\alpha_h^2\beta_h^2\gamma_{\text{th}}}{16N^2A_0^2}\right)^{b_k}\bar{\gamma}^{-\left(\frac{1}{2}+b_k\right)}\ .\tag{44}$$

$$\begin{aligned}P_{\substack{\text{out}\\ \bar{\gamma}\to\infty}}\left(\bar{\gamma}\right) = &\frac{2^{\alpha_h+\beta_h-5}\alpha_h\beta_h\xi^2\gamma_{\text{th}}^{\frac{1}{2}}\prod_{j=1,b_j\neq\min(\mathbf{b})}^{6}\Gamma\left(b_j-\min\left(\mathbf{b}\right)\right)}{\pi N\Gamma\left(\alpha_h\right)\Gamma\left(\beta_h\right)A_0\left(\frac{1}{2}+\min\left(\mathbf{b}\right)\right)\Gamma\left(\frac{\xi^2}{2}-\min\left(\mathbf{b}\right)\right)\Gamma\left(\frac{\xi^2+1}{2}-\min\left(\mathbf{b}\right)\right)}\\ &\times\left(\frac{\alpha_h^2\beta_h^2\gamma_{\text{th}}}{16N^2A_0^2}\right)^{\min(\mathbf{b})}\bar{\gamma}^{-\left(\frac{1}{2}+\min(\mathbf{b})\right)}\ .\end{aligned}\tag{45}$$

Substituting (27) and (54) into (53), we obtain the integral equation as (55) shown at the bottom of this page. By applying Eq. (07.34.21.0013.01) in [38] for the integration of the product of two Meijer-G functions in (55), we obtain the closed-form expression of the ergodic channel capacity as (56) shown at the bottom of this page.

IV. Simulation Results

In this section, we verify the derived closed-form expressions through Monte Carlo simulation. Unless otherwise stated, we consider threshold SNR $\gamma_{th} = 15$ dB, detector aperture diameter $D_R = 5$ cm, noise variance $\sigma_n^2 = -100$ dBm, the reflection coefficient of reflecting elements $\rho = 1$, the extinction coefficient $c = 0.15\ \mathrm{m}^{-1}$, wavelength $\lambda = 530$ nm, the link distance $L_1 = L_2 = 50$ m, the dissipation rate of mean-squared temperature [32] $\chi_{T_1} = \chi_{T_2} = 1 \times 10^{-5}\ \mathrm{K}^2 \cdot \mathrm{s}^{-3}$, the Kolmogorov microscale length [32] $\eta_1 = \eta_2 = 7.5 \times 10^{-5}$, the dissipation rate of turbulent kinetic energy per unit mass of fluid [32] $\varepsilon_1 = 3 \times 10^{-2}\ \mathrm{m}^2 \cdot \mathrm{s}^{-3}$ and $\varepsilon_2 = 5 \times 10^{-4}\ \mathrm{m}^2 \cdot \mathrm{s}^{-3}$. Based on these parameters, the turbulence parameters are set to $\alpha = 4.37$ and $\beta = 1.24$.

We first confirm the accuracy of the approximate distribution of the sum of Gamma-Gamma random variables, i.e., $h_t = \sum_{n=1}^{N} h_{tn} \sim \Gamma\Gamma(\alpha_h, \beta_h, N)$. In Fig. 2, we give the exact cumulative distribution function (CDF) and the approximate CDF for different numbers of reflecting elements. The exact CDF is the empirical CDF based on the sum of the N i.i.d randomly generated Gamma-Gamma random variables from (6), while the approximate CDF is the empirical CDF based on the randomly generated Gamma-Gamma random variables from (17). From Fig. 2, it can be found that the approximate CDFs are well-matched with the exact CDFs. Further, Kolmogorov Smirnov statistic [43] is used as goodness of fit. This quantifies the vertical distance between the approximate CDF and the exact CDF, and the distance should not be greater than the so-called maximum difference D_m. For 1×10^4 samples we used, $D_m = 0.0136$ and confidence level of 0.05 are usually selected [43]. We find that the distance is smaller than D_m for different numbers of reflecting elements. Therefore, it can be concluded that the approximate distribution we applied is accurate.

In Fig. 3, we analyze the outage probability performance of the RIS-assisted UWOC system with different numbers of reflecting elements. We consider the number of reflecting elements of $N = 2,\ 4,\ 8,\ 16,\ 24,\ 32,\ 40,\ 48,\ 56$. It can be observed from Fig. 3 that the analysis results in our derived closed-form expression of (30) are consistent with the simulation results, which verifies the accuracy of the derivation. Even if the number of reflection elements is small, such as $N = 2$ and $N = 4$, our results still accurately evaluate the system performance. From Fig. 3, the outage probability decreases with the increase in the number of reflecting elements of RIS. For example, SNR of $\bar{\gamma} = 21$ dB is required for $N = 8$ in order to achieve a target outage probability of $P_{\mathrm{out}} = 10^{-3}$. The SNR decreases to 13.8 dB, 9.7 dB and 7 dB, and an extra SNR of 7.2 dB, 11.3 dB and 14 dB is required for $N = 16$, $N = 24$ and $N = 32$. It can also be shown from Fig. 3 that when the number of IRS reflecting elements reaches a certain number, the outage probability performance of the UWOC system is significantly improved. However, the outage probability performance will improve more slowly with the increase in the number of reflecting elements. This is also consistent with the results in Fig. 4. From Fig. 4, the outage probability decreases with the increase of N, but the decline speed becomes slower. The outage probability performance gain $G(N)$ also decreases with the increase in the number of reflecting elements. When the number of reflective elements is relatively large, $G(N)$ tends to be stable. Although $G(N)$ tends to be stable with the increase of N, the value of $G(N)$ is always greater than 1, i.e., $G(N) > 1$. This means that the outage probability always decreases with the increase of N. Therefore, it can be concluded that when $N \to \infty$, the outage probability approaches zero. This is consistent with our analysis of $P_{\mathrm{out}}(N)_{N\to\infty}$.

$$\mathrm{CS}\left(\bar{\gamma}\right) = \left\{ 2\left[\mathrm{G}_{4,8}^{6,2}\left(\frac{\alpha_{\mathrm{h}}^2 \beta_{\mathrm{h}}^2 \gamma_{\mathrm{th}}}{16\mathrm{N}^2 \mathrm{A}_0^2 \bar{\gamma}} \middle| \begin{matrix} 0, \frac{1}{2}, \frac{\xi^2}{2}, \frac{\xi^2+1}{2} \\ \mathbf{b}, 1, -\frac{1}{2} \end{matrix} \right) \right]^2 - 2\mathrm{G}_{5,9}^{6,3}\left(\frac{\alpha_{\mathrm{h}}^2 \beta_{\mathrm{h}}^2 \gamma_{\mathrm{th}}}{16\mathrm{N}^2 \mathrm{A}_0^2 \bar{\gamma}} \middle| \begin{matrix} 0, 0, \frac{1}{2}, \frac{\xi^2}{2}, \frac{\xi^2+1}{2} \\ \mathbf{b}, 1, 1, -\frac{1}{2} \end{matrix} \right) \right.$$
$$\left. \times G_{3,7}^{6,1}\left(\frac{\alpha_h^2 \beta_h^2 \gamma_{\mathrm{th}}}{16N^2 A_0^2 \bar{\gamma}} \middle| \begin{matrix} \frac{1}{2}, \frac{\xi^2}{2}, \frac{\xi^2+1}{2} \\ \mathbf{b}, -\frac{1}{2} \end{matrix} \right) \right\} \Big/ \left\{ \min\left(\xi^2, \alpha_h, \beta_h\right) \left[G_{3,7}^{6,1}\left(\frac{\alpha_h^2 \beta_h^2 \gamma_{\mathrm{th}}}{16N^2 A_0^2 \bar{\gamma}} \middle| \begin{matrix} \frac{1}{2}, \frac{\xi^2}{2}, \frac{\xi^2+1}{2} \\ \mathbf{b}, -\frac{1}{2} \end{matrix} \right) \right]^2 \right\}. \tag{52}$$

$$C = \frac{\alpha_h \beta_h \xi^2}{2\ln(2) N \Gamma\left(\alpha_h\right) \Gamma\left(\beta_h\right) A_0 \bar{\gamma}^{\frac{1}{2}}} \int_0^{\infty} \gamma^{-\frac{1}{2}} G_{2,2}^{1,2}\left(\tau\gamma \middle| \begin{matrix} 1, 1 \\ 1, 0 \end{matrix} \right) G_{1,3}^{3,0}\left(\frac{\alpha_h \beta_h}{N A_0 \bar{\gamma}^{\frac{1}{2}}} \gamma^{\frac{1}{2}} \middle| \begin{matrix} \xi^2 \\ \xi^2 - 1, \alpha_h - 1, \beta_h - 1 \end{matrix} \right) d\gamma\,. \tag{55}$$

$$C = \frac{2^{\alpha_h + \beta_h - 5} \alpha_h \beta_h \xi^2}{\ln(2) \pi N \Gamma\left(\alpha_h\right) \Gamma\left(\beta_h\right) A_0 \tau^{\frac{1}{2}} \bar{\gamma}^{\frac{1}{2}}} G_{4,8}^{8,1}\left(\frac{\alpha_h^2 \beta_h^2}{16N^2 A_0^2 \tau \bar{\gamma}} \middle| \begin{matrix} -\frac{1}{2}, \frac{1}{2}, \frac{\xi^2}{2}, \frac{\xi^2+1}{2} \\ \mathbf{b}, -\frac{1}{2}, -\frac{1}{2} \end{matrix} \right). \tag{56}$$

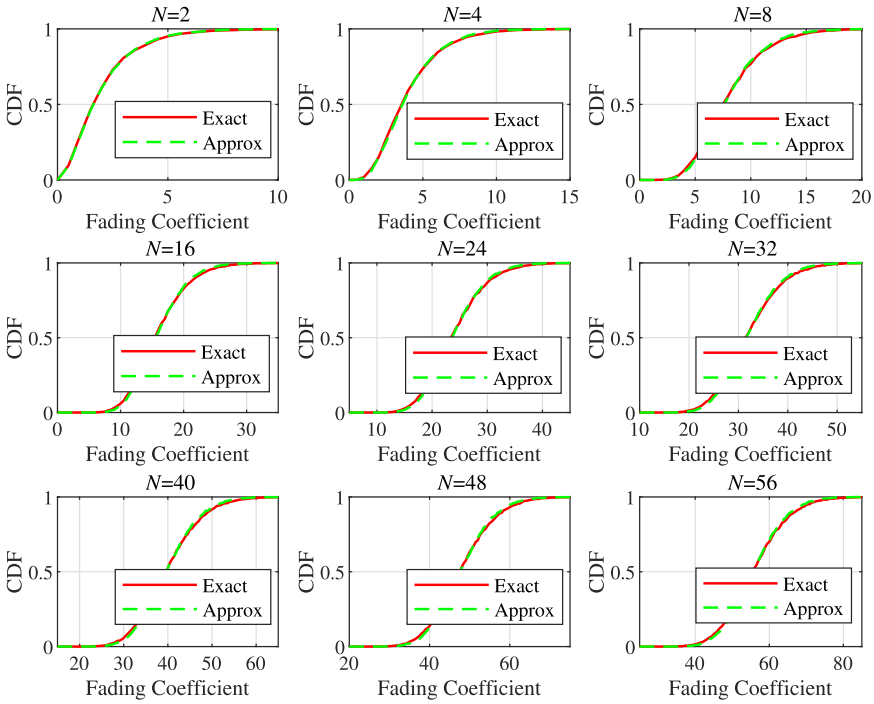

Fig. 2. Exact and approximate CDFs for different numbers of reflecting elements.

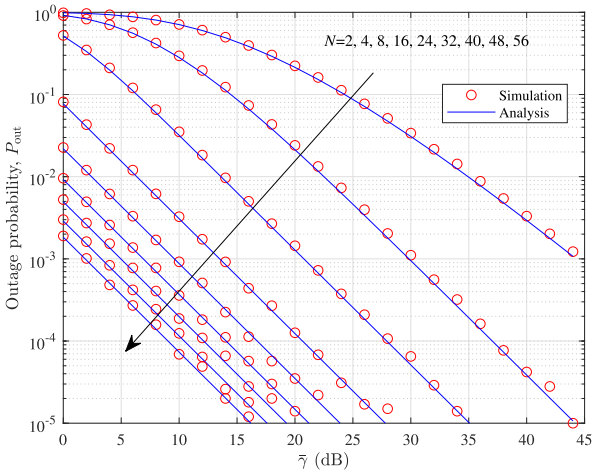

Fig. 3. Outage probability with different numbers of reflecting elements. Here, $\sigma_\theta = 2 \times 10^{-3}, \sigma_\phi = 1.5 \times 10^{-3}$.

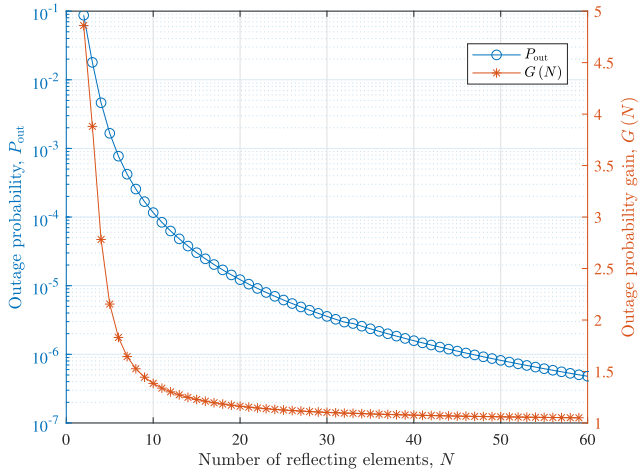

Fig. 4. The relationship between the outage probability and the number of reflecting elements. Here, $\sigma_\theta = 2 \times 10^{-3}, \sigma_\phi = 1.5 \times 10^{-3}$ and $\bar{\gamma} = 25$ dB.

In Fig. 5, we consider the outage probability with different jitter values. Outage probability is obtained based on (30) and, as expected, it is well matched with the simulation results. Our results further quantify the outage probability performance degradation associated with the increase in pointing errors caused by the increase in jitter values. It is observed from Fig. 5 that the increase in σ_θ and σ_ϕ will all lead to the deterioration of outage probability performance. For instance, SNR of $\bar{\gamma} = 10$ dB is required in order to achieve a target outage probability of $P_{\text{out}} = 10^{-3}$ when $\sigma_\theta = 1 \times 10^{-3}$ and $\sigma_\phi = 1 \times 10^{-3}$. The required SNR climbs to 12.5 dB and 17 dB, indicating an extra SNR of 2.5 dB and 7 dB if σ_θ increases to 1.5×10^{-3} and 2×10^{-3}. Similarly, when $\sigma_\theta = 2 \times 10^{-3}$ and $\sigma_\phi = 1.5 \times 10^{-3}$, the targeted outage probability can be achieved with $\bar{\gamma} = 20.8$ dB. And As σ_ϕ increases to 2×10^{-3} and 2.5×10^{-3}, the required SNR raises to 26 dB and 34 dB with an extra SNR of 5.2 dB and 13.2 dB.

In Fig. 6, we present the diversity order with different numbers of reflecting elements, and verify the closed-form expressions for the finite-SNR diversity order in (42) and the asymptotical diversity order in (46), respectively. As a benchmark, we include the finite-SNR diversity order given by numerical evaluation in

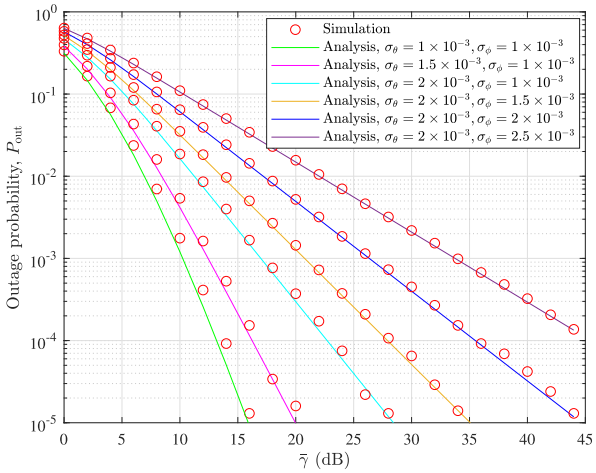

Fig. 5. Outage probability with different jitter values. Here, $N = 8$.

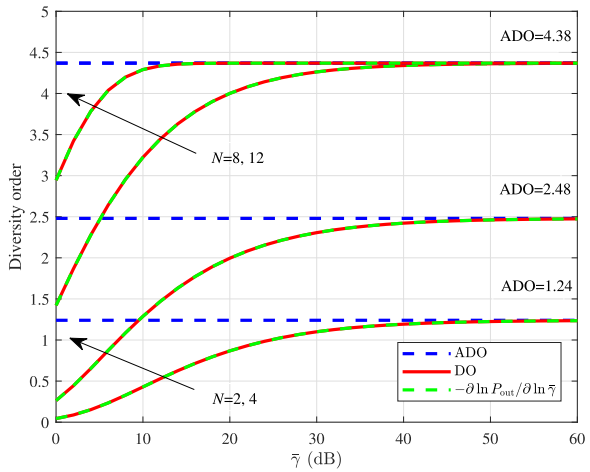

Fig. 6. Diversity order with different numbers of reflecting elements. Here, $\sigma_\theta = 1\times10^{-3}, \sigma_\phi = 1\times10^{-3}$.

(37). The plot shows that our derived closed-form expression for the finite-SNR diversity order in (42) provides an exact match to the diversity order in (37). This proves the correctness of our derivation. At a lower SNR level, the finite-SNR diversity order increases with the increase in SNR and the number of reflecting elements. For example, the finite-SNR diversity order at 10 dB is given as 0.43, 1.29, 3.22 and 4.29 for the numbers of reflecting elements of $N = 2,\ 4,\ 8,\ 12$. At a higher SNR level, the diversity order does not change significantly with the increase in SNR. It reaches the upper limit of the diversity order, i.e., the asymptotical diversity order obtained by (46). In this scenario, the asymptotical diversity order depends on the number of reflecting elements, the turbulence parameters, and the pointing errors. Here, we set $\sigma_\theta = 1\times10^{-3}, \sigma_\phi = 1\times10^{-3}$, then ξ^2 is calculated as 8.76. According to (46), when $N = 2$ and 4, we obtain $N\beta < \xi^2$. In this case, the asymptotical diversity order depends on the number of reflecting elements and the turbulence parameter, and $\text{ADO} = \frac{1}{2}\min(\xi^2, N\alpha, N\beta) = \frac{1}{2}N\beta = 1.24$ and 2.48. Continue to increase the number of reflecting elements, such as $N = 8,\ 12$, we have $\xi^2 < N\beta$ and the asymptotical diversity order depends on the pointing error, then $\text{ADO} = \frac{1}{2}\min(\xi^2, N\alpha, N\beta) = \frac{1}{2}\xi^2 = 4.38$. Therefore, when the number of reflecting elements of N reaches a specific value, if we continue to increase N, the diversity order performance will not be improved.

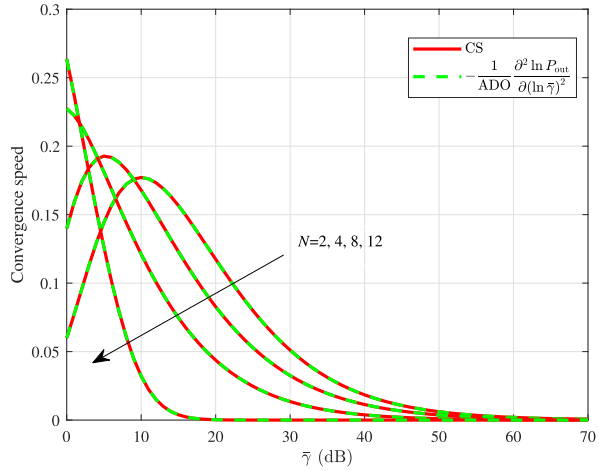

Fig. 7. Convergence speed with different numbers of reflecting elements. Here, $\sigma_\theta = 1\times10^{-3}, \sigma_\phi = 1\times10^{-3}$.

In Fig. 7, we show the convergence speed of the finite-SNR diversity order to the asymptotical diversity order. Similar to Fig. 6, a perfect match can be observed between the convergence speed expression derived in (52) and its numerical calculation based on (47). With the increase in SNR, the convergence speed gradually tends to zero, which indicates that the finite-SNR diversity order has reached the asymptotical diversity order. It is further observed that the more reflecting elements, the faster convergence to the asymptotical diversity order. Although the systems with $N = 8$ and $N = 12$ have the same asymptotical diversity order in Fig. 6, the system with $N = 12$ converges faster, i.e., it can reach the asymptotical diversity order under lower SNR.

In Fig. 8, we investigate the diversity order with different jitter values. In Fig. 9, we show the corresponding convergence speed. With the increase in jitter values, the effect of the pointing error becomes larger, which leads to the reduction of finite-SNR diversity order. For example, when $\sigma_\theta = 1\times10^{-3}$ and $\sigma_\phi = 1\times10^{-3}$, the finite-SNR diversity order is 2.0 at $\bar{\gamma} = 20$ dB. If σ_θ increases to 1.5×10^{-3} and 2×10^{-3}, the finite-SNR diversity order falls to 1.84 and 1.51. Additionally, if we set $\sigma_\phi = 1\times10^{-3}$, the same asymptotical diversity order is obtained when $\sigma_\theta = 1\times10^{-3}$ and 1.5×10^{-3}. In the two cases, ξ^2 can be calculated as 8.76 and 5.38, and $N\beta < \xi^2$, the asymptotical diversity order depends on the value of $N\beta$, then we obtain $\text{ADO} = \frac{1}{2}\min(\xi^2, N\alpha, N\beta) = \frac{1}{2}N\beta = 2.48$. Although they have the same asymptotical diversity order, the convergence speed of the system with $\sigma_\theta = 1.5\times10^{-3}$ is slower

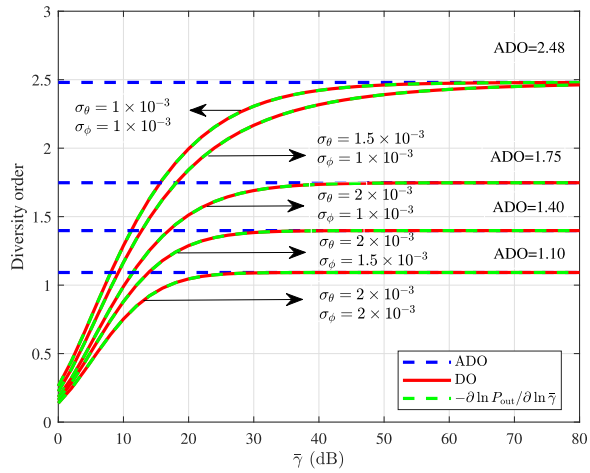

Fig. 8. Diversity order with different jitter values. Here, $N = 4$.

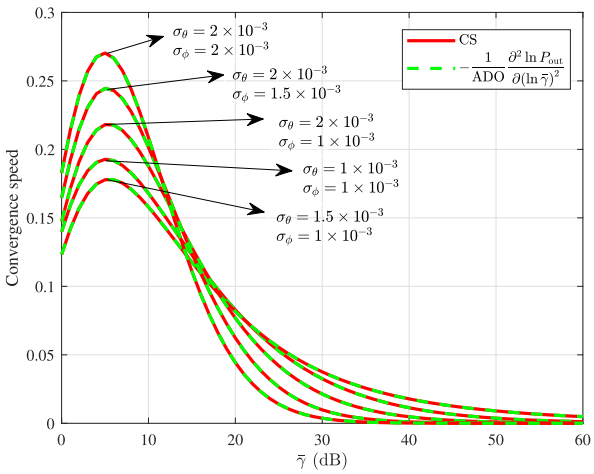

Fig. 9. Convergence speed with different jitter values. Here, $N = 4$.

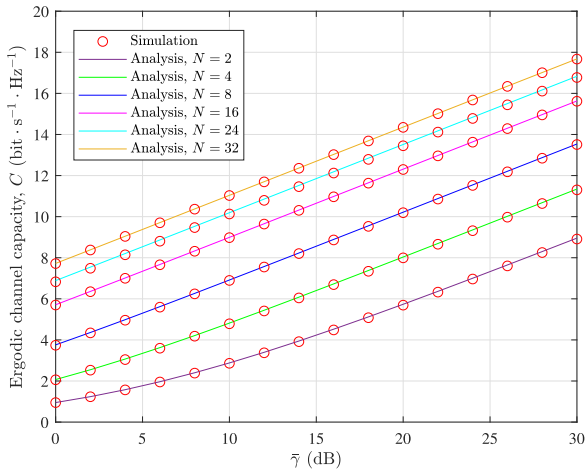

Fig. 10. Ergodic channel capacity with different numbers of reflecting elements. Here, $\sigma_\theta = 2 \times 10^{-3}, \sigma_\phi = 1.5 \times 10^{-3}$.

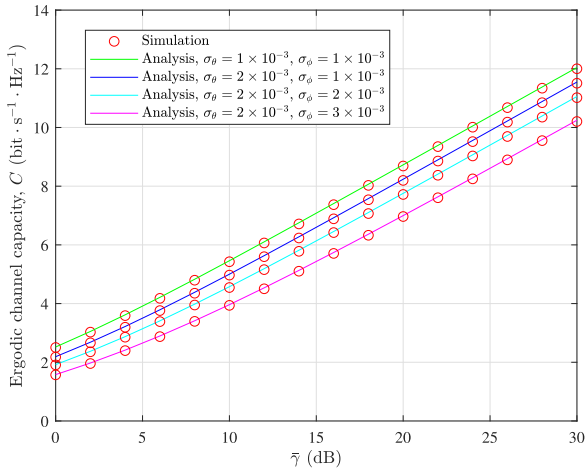

Fig. 11. Ergodic channel capacity with different jitter values. Here, $N = 4$.

in Fig. 9. In Figs. 8 and 9, as the jitter value increases, the asymptotical diversity order decreases, and the convergence speed becomes faster. Because we have $\xi^2 < N\beta$, and the asymptotical diversity order depends on the value of ξ^2. At this time, according to (46) and (52), it can also be obtained that the decrease in ξ^2 can lead to the decrease in the asymptotical diversity order and the increase in the convergence speed. To sum up, we can draw insightful conclusions. When the asymptotical diversity order is dominated by the number of reflecting elements and the minimum turbulence parameter, i.e., $\xi^2 > N \min(\alpha, \beta)$, the increase in pointing error level will not change the asymptotical diversity order. However, it can reduce the finite-SNR diversity order and the convergence speed. When the asymptotical diversity order is dominated by the pointing error, i.e., $\xi^2 < N \min(\alpha, \beta)$, the increase in the pointing error level will reduce the finite-SNR diversity order and the asymptotical diversity order, while the convergence speed will increase.

In Fig. 10, we investigate the ergodic channel capacity with different numbers of reflecting elements. The simulation results match well with the analysis results of (56), which verifies the accuracy of the derivation of ergodic capacity. We can find that increasing the number of reflecting elements can significantly improve the ergodic capacity. For example, the ergodic capacity is 5.74 bit $\cdot$ s^{-1} $\cdot$ Hz^{-1} at $\bar{\gamma} = 20$ dB when $N = 2$. However, when $N = 4,\ 8,\ 16,\ 24,\ 32$, the ergodic capacity is increased to 7.99, 10.19, 12.30, 13.45 and 14.35 bit $\cdot$ s^{-1} $\cdot$ Hz^{-1} at $\bar{\gamma} =$ 20 dB, respectively. It can also be observed that for the cases of $N = 8,\ 16,\ 24,\ 32$, the increment of ergodic capacity decreases with the increase of N at the same SNR. In other words, the increase speed of ergodic capacity slows down.

In Fig. 11, we propose the ergodic channel capacity with different jitter values. Under different jitter values, i.e., different pointing error levels, the simulation results are consistent with the analysis results in (56). It can be observed from Fig. 11 that the increase in pointing errors can lead to the degradation of ergodic capacity performance. For instance, when $\sigma_\theta = 1 \times 10^{-3}$ and $\sigma_\phi = 1 \times 10^{-3}$, the ergodic capacity is 8.69 bit $\cdot$ s^{-1} $\cdot$ Hz^{-1} at $\bar{\gamma} = 20$ dB. The ergodic capacity reduces to 8.19 bit $\cdot$ s^{-1} $\cdot$ Hz^{-1} if σ_θ increases to 2×10^{-3}, and the ergodic

capacity is reduced by 5.75%. Similarly, when $\sigma_\theta = 2 \times 10^{-3}$ and σ_ϕ increases from 1×10^{-3} to 2×10^{-3} and 3×10^{-3}, the ergodic capacity at $\bar{\gamma} = 20$ dB decreases from 8.19 to 7.72 and 6.97 $\text{bit} \cdot \text{s}^{-1} \cdot \text{Hz}^{-1}$, which is decreased by 5.74% and 14.90%.

V. Conclusion

In this paper, we investigated a RIS-assisted UWOC system with IM-DD in an underwater environment with obstacles. The cascaded turbulence channel fading coefficients from source to destination through RIS are modeled as Gamma-Gamma distribution, and the pointing error caused by beam jitter and RIS jitter has been considered. The probability density function of instantaneous received SNR is proposed by using the approximate distribution of the sum of Gamma-Gamma random variables, and the novel closed-form expression of outage probability is derived. Then, based on the outage probability result, the finite-SNR diversity order, the asymptotical diversity order, and the convergence speed of finite-SNR diversity order to asymptotical diversity order have been analyzed. Furthermore, the ergodic channel capacity is also investigated. Finally, the simulation results are presented to confirm the accuracy of our derivations. Analytical and simulation results show that increasing the number of reflecting elements improves the outage probability performance and the ergodic channel capacity, while the pointing error deteriorates the system performance. When the number of reflecting elements is very large (i.e., tends to infinity), the outage probability asymptotically approaches zero. Additionally, appropriately increasing the number of reflecting elements can improve the finite-SNR diversity order and its convergence speed, and the asymptotical diversity order depends on the number of reflecting elements, the pointing error, and the minimum turbulence parameter.

References

[1] R. A. Khalil, N. Saeed, M. I. Babar, and T. Jan, "Toward the Internet of Underwater Things: Recent developments and future challenges," *IEEE Consum. Electron. Mag.*, vol. 10, no. 6, pp. 32–37, Nov. 2021.

[2] Z. Liu, X. Meng, Y. Liu, Y. Yang, and Y. Wang, "AUV-aided hybrid data collection scheme based on value of information for Internet of Underwater Things," *IEEE Internet Things J.*, vol. 9, no. 9, pp. 6944–6955, May 2022.

[3] S. A. H. Mohsan, Y. L. Li, M. Sadiq, J. W. Liang, and M. A. Khan, "Recent advances, future trends, applications and challenges of Internet of Underwater Things (IoUT): A comprehensive review," *J. Mar. Sci. Eng.*, vol. 11, no. 1, Jan. 2023, Art. no. 124.

[4] Z. Zeng, S. Fu, H. Zhang, Y. Dong, and J. Cheng, "A survey of underwater optical wireless communications," *IEEE Commun. Surveys Tuts.*, vol. 19, no. 1, pp. 204–238, Firstquarter 2017.

[5] M. F. Ali, D. N. K. Jayakody, and Y. Li, "Recent trends in underwater visible light communication (UVLC) systems," *IEEE Access*, vol. 10, pp. 22169–22225, 2022.

[6] H. Lei, Y. Zhang, K.-H. Park, I. S. Ansari, G. Pan, and M.-S. Alouini, "Performance analysis of dual-hop RF-UWOC systems," *IEEE Photon. J.*, vol. 12, no. 2, Apr. 2020, Art. no. 7901915.

[7] Y. Lou, R. Sun, J. Cheng, D. Nie, and G. Qiao, "Secrecy outage analysis of two-hop decode-and-forward mixed RF/UWOC systems," *IEEE Commun. Lett.*, vol. 26, no. 5, pp. 989–993, May 2022.

[8] H. Lei, C. Zhu, I. S. Ansari, K.-H. Park, and G. Pan, "Secrecy outage performance analysis of dual-hop RF-UOWC systems," *IEEE Syst. J.*, vol. 17, no. 2, pp. 2133–2144, Jun. 2023.

[9] Q. Wu and R. Zhang, "Towards smart and reconfigurable environment: Intelligent reflecting surface aided wireless network," *IEEE Commun. Mag.*, vol. 58, no. 1, pp. 106–112, Jan. 2020.

[10] E. Basar, M. Di Renzo, J. De Rosny, M. Debbah, M.-S. Alouini, and R. Zhang, "Wireless communications through reconfigurable intelligent surfaces," *IEEE Access*, vol. 7, pp. 116753–116773, 2019.

[11] D.-W. Yue, H. H. Nguyen, and Y. Sun, "mmWave doubly-massive-MIMO communications enhanced with an intelligent reflecting surface: Asymptotic analysis," *IEEE Access*, vol. 8, pp. 183774–183786, 2020.

[12] Z. Wang, Z. Liu, Y. Shen, A. Conti, and M. Z. Win, "Location awareness in beyond 5G networks via reconfigurable intelligent surfaces," *IEEE J. Sel. Areas Commun.*, vol. 40, no. 7, pp. 2011–2025, Jul. 2022.

[13] A. Shojaeifard et al., "MIMO evolution beyond 5G through reconfigurable intelligent surfaces and fluid antenna systems," *Proc. IEEE*, vol. 110, no. 9, pp. 1244–1265, Sep. 2022.

[14] Z. Chen et al., "Reconfigurable-intelligent-Surface-Assisted B5G/6G wireless communications: Challenges, solution, and future opportunities," *IEEE Commun. Mag.*, vol. 61, no. 1, pp. 16–22, Jan. 2023.

[15] S. Sun, T. Wang, F. Yang, J. Song, and Z. Han, "Intelligent reflecting surface-aided visible light communications: Potentials and challenges," *IEEE Veh. Technol. Mag.*, vol. 17, no. 1, pp. 47–56, Mar. 2022.

[16] A. M. Abdelhady, O. Amin, A. K. S. Salem, M.-S. Alouini, and B. Shihada, "Channel characterization of IRS-Based visible light communication systems," *IEEE Trans. Commun.*, vol. 70, no. 3, pp. 1913–1926, Mar. 2022.

[17] S. Sun, F. Yang, J. Song, and Z. Han, "Joint resource management for intelligent reflecting surface-aided visible light communications," *IEEE Trans. Wireless Commun.*, vol. 21, no. 8, pp. 6508–6522, Aug. 2022.

[18] S. Sun, F. Yang, J. Song, and Z. Han, "Optimization on multiuser physical layer security of intelligent reflecting surface-aided VLC," *IEEE Wirel. Commun. Lett.*, vol. 11, no. 7, pp. 1344–1348, Jul. 2022.

[19] R. K. Pal, S. P. Dash, S. Aïssa, and D. Ghose, "Outage probability analysis of RIS-Assisted indoor Wide-FOV-VLC/RF wireless communication," *IEEE Wirel. Commun. Lett.*, vol. 13, no. 1, pp. 34–38, Jan. 2024.

[20] A. R. Ndjiongue, T. M. N. Ngatched, O. A. Dobre, and H. Haas, "Reconfigurable intelligent surface-based VLC receivers using tunable liquid-crystals: The concept," *J. Lightw. Technol.*, vol. 39, no. 10, pp. 3193–3200, May 2021.

[21] S. Aboagye, A. R. Ndjiongue, T. M. N. Ngatched, and O. A. Dobre, "Design and optimization of liquid crystal RIS-based visible light communication receivers," *IEEE Photon. J.*, vol. 14, no. 6, Dec. 2022, Art. no. 7355607.

[22] L. Yang, W. Guo, D. B. da Costa, and M.-S. Alouini, "Free-space optical communication with reconfigurable intelligent surfaces," 2020, *arXiv:2012.00547*.

[23] A. R. Ndjiongue, T. M. N. Ngatched, O. A. Dobre, A. G. Armada, and H. Haas, "Analysis of RIS-Based Terrestrial-FSO link over G-G turbulence with distance and jitter ratios," *J. Lightw. Technol.*, vol. 39, no. 21, pp. 6746–6758, Nov. 2021.

[24] H. Wang et al., "Performance analysis of multi-branch reconfigurable intelligent surfaces-assisted optical wireless communication system in environment with obstacles," *IEEE Trans. Veh. Technol.*, vol. 70, no. 10, pp. 9986–10001, Oct. 2021.

[25] N. Vishwakarma and R. Swaminathan, "Performance analysis of multiple optical reflecting surfaces assisted FSO communication," in *Proc. IEEE Wireless Commun. Netw. Conf.*, 2023, pp. 1–6.

[26] R. P. Naik and W.-Y. Chung, "Evaluation of reconfigurable intelligent surface-assisted underwater wireless optical communication system," *J. Lightw. Technol.*, vol. 40, no. 13, pp. 4257–4267, Jul. 2022.

[27] Y. Ata, H. Abumarshoud, L. Bariah, S. Muhaidat, and M. A. Imran, "Intelligent reflecting surfaces for underwater visible light communications," *IEEE Photon. J.*, vol. 15, no. 1, Feb. 2023, Art. no. 7300609.

[28] S. Li, L. Yang, D. B. d. Costa, M. D. Renzo, and M.-S. Alouini, "On the performance of RIS-Assisted dual-hop mixed RF-UWOC systems," *IEEE Trans. Cogn. Commun. Netw.*, vol. 7, no. 2, pp. 340–353, Jun. 2021.

[29] C. Li, K.-H. Park, and M.-S. Alouini, "On the use of a direct radiative transfer equation solver for path loss calculation in underwater optical wireless channels," *IEEE Wireless Commun. Lett.*, vol. 4, no. 5, pp. 561–564, Oct. 2015.

[30] I. C. Ijeh, M. A. Khalighi, M. Elamassie, S. Hranilovic, and M. Uysal, "Outage probability analysis of a vertical underwater wireless optical link subject to oceanic turbulence and pointing errors," *IEEE J. Opt. Commun. Netw.*, vol. 14, no. 6, pp. 439–453, Jun. 2022.

[31] M. A. Al-Habash, L. C. Andrews, and R. L. Phillips, "Mathematical model for the irradiance probability density function of a laser beam propagating through turbulent media," *Opt. Eng.*, vol. 40, no. 8, pp. 1554–1562, 2001.

[32] M. Elamassie, M. Uysal, Y. Baykal, M. Abdallah, and K. Qaraqe, "Effect of eddy diffusivity ratio on underwater optical scintillation index," *J. Opt. Soc. Amer. A*, vol. 34, no. 11, pp. 1969–1973, Nov. 2017.

[33] A. A. Farid and S. Hranilovic, "Outage capacity optimization for free-space optical links with pointing errors," *J. Lightw. Technol.*, vol. 25, no. 7, pp. 1702–1710, Jul. 2007.
[34] M. Elamassie and M. Uysal, "Asymptotic performance of generalized transmit laser selection over lognormal turbulence channels," *IEEE Commun. Lett.*, vol. 24, no. 8, pp. 1762–1766, Aug. 2020.
[35] Z. Rahman, N. V. Tailor, S. M. Zafaruddin, and V. K. Chaubey, "Unified performance assessment of optical wireless communication over multilayer underwater channels," *IEEE Photon. J.*, vol. 14, no. 5, Oct. 2022, Art. no. 7349114.
[36] M. R. Bhatnagar and Z. Ghassemlooy, "Performance analysis of gamma-gamma fading FSO MIMO links with pointing errors," *J. Lightw. Technol.*, vol. 34, no. 9, pp. 2158–2169, May 2016.
[37] T. V. Pham, T. C. Thang, and A. T. Pham, "Average achievable rate of spatial diversity MIMO-FSO over correlated gamma-gamma fading channels," *IEEE J. Opt. Commun. Netw.*, vol. 10, no. 8, pp. 662–674, Aug. 2018.
[38] "Wolfram research," Accessed: Jan. 30, 2024. [Online]. Available: http://functions.wolfram.com
[39] S. Tang, X. Zhang, and Y. Dong, "Temporal statistics of irradiance in moving turbulent ocean," in *Proc. IEEE MTS/IEEE OCEANS*, 2013, pp. 1–4.
[40] M. Elamassie and M. Uysal, "Outage performance analysis of vertical underwater VLC links," in *Proc. IEEE 30th Signal Process. Commun. Appl. Conf.*, 2022, pp. 1–5.
[41] S. Loyka and G. Levin, "Diversity-multiplexing tradeoff via asymptotic analysis of large MIMO systems," in *Proc. IEEE Int. Symp. Inf. Theory*, 2007, pp. 2826–2830.
[42] M. Elamassie, S. M. Sait, and M. Uysal, "Finite-SNR diversity gain analysis of FSO systems over gamma-gamma fading channels with pointing errors," *IEEE Commun. Lett.*, vol. 25, no. 6, pp. 1940–1944, Jun. 2021.
[43] M. Lovric, *International Encyclopedia of Statistical Science*. New York, NY, USA: Springer, 2010.